

1 **Simultaneous removal of heavy metals and dyes in water using a MgO-coated Fe₃O₄**
2 **nanocomposite: Role of micro-mixing effect induced by bubble generation**

3
4 Manoj P. Rayaroth ^{a, b}, Dasom Oh ^a, Chung-Seop Lee ^a, Yoon-Seok Chang ^{a*}

5 ^a Division of Environmental Science and Engineering, Pohang University of Science and
6 Technology (POSTECH), Nam-gu, Pohang, 37673, Republic of Korea.

7 ^b Department of Process Engineering and Chemical Technology, Faculty of Chemistry, Gdansk
8 University of Technology, 80-233 Gdańsk, 11/12 Narutowicza Str, Poland

9
10
11
12 * **Corresponding author**

13 **Prof. Dr. Yoon-Seok Chang**

14 Division of Environmental Science and Engineering

15 Pohang University of Science and Technology (POSTECH)

16 Pohang 37673, Republic of Korea

17 Tel.: +82 54 279 2281; Fax: +82 54 279 8299

18 Email address: chang.yoonseok@postech.ac.kr

19 **Abstract:**

20 This study focused on the development of a nano-adsorbent for contaminant removal
21 without the use of any external energy. An eco-friendly Fe₃O₄@MgO core-shell nanocomposite
22 was synthesized and tested for the removal of a heavy metal, lead (Pb²⁺) and a dye, rhodamine B
23 (RhB). The addition of H₂O₂ into the system enabled the self-mixing of the aqueous solution
24 containing Fe₃O₄@MgO through the generation of bubbles. This system showed an excellent
25 removal efficiency of 99% in just 15 min for Pb²⁺ and 120 min for RhB, which is far better than
26 the control experiment (without H₂O₂). The cation exchange mechanism dominated in the
27 removal of heavy metals, while the adsorptive removal of dye proceeded through the H-bonding
28 between Mg(OH)₂ and dye molecules. The removal efficiency increased exponentially with the
29 increase of H₂O₂ at the optimal concentration of 5% and it was effective over a wide pH range.
30 Moreover, the performance of the Fe₃O₄@MgO-H₂O₂ system was verified for other heavy metals
31 such as Cd, Ni, Zn, Co, and Cu, demonstrating that the Fe₃O₄@MgO-H₂O₂ system can be widely
32 implemented in the treatment of real water matrices contaminated with heavy metals and organic
33 dyes.

34 **Keywords:** *Water treatment, Fe₃O₄@MgO, bubble generation, adsorption, heavy metals, dyes*

35



36 ***Abbreviations***

37 RhB: rhodamine B, PEG: Polyethylene glycol, CTAB: Cetyltrimethylammonium bromide,
38 SEM: scanning electron microscopy, EDX: Energy dispersive X-ray, XRD: X-ray diffractometer,
39 XPS: X-ray photoelectron spectroscopy, ICP-OES: inductively coupled plasma–optical emission
40 spectrometer, DO: Dissolved oxygen

41

42

Journal Pre-proof

43 1. Introduction

44 Heavy metals such as arsenic, lead, cadmium, nickel, chromium, cobalt, and selenium are
45 major environmental pollutants because of their toxic effects, even at trace levels (Nadeem et al.,
46 2006; Qiu et al., 2021). All these elements are discharged directly from industries and agricultural
47 fields into the aquatic system. Their adverse effects create negative impacts on all environmental
48 compartments (Vakili et al., 2014). Although there are several sources of the exposure of humans
49 to these pollutants, their intake via drinking water is the most prominent and thereby highlights
50 the need for a proper treatment protocol. Another important category of water pollutants is dye
51 waste (Nigam et al., 1996) which is introduced into water bodies from textile mills, leather, jute,
52 and food industries. Previous reports showed that dyehouse effluent contains many heavy metals,
53 which also increase the perilous situation of water pollution by this kind of waste (Chen et al.,
54 2007; Ye et al., 2021b). However, traditional technologies such as ion exchange, biological
55 degradation, reverse osmosis, coagulation and flocculation, membrane filtration, oxidation, and
56 chemical precipitation are effective mostly in the removal of a single pollutant from various
57 contaminated water (Dotto et al., 2019; Rasaki et al., 2019; Zazou et al., 2019; Iqbal et al., 2021).
58 Therefore, recent studies have focused on the materials/methods that could remove both heavy
59 metals and organic pollutants in water (Kim et al., 2018; Ghaedi et al., 2022; Malik et al., 2022).

60 Adsorption using various nanomaterials is the most frequently used technique for the
61 removal of a majority of pollutants (Valix et al., 2004; Afroze and Sen, 2018; Abdullah et al.,
62 2019; Joseph et al., 2019; Castro-Muñoz et al., 2021; Osagie et al., 2021). However, it was found
63 not to be very effective, especially when dealing with a mixture of pollutants. Therefore, the
64 selection of an adsorbent that is capable of removing both organic and inorganic pollutants is a
65 typical challenge in this field. Another difficulty is the requirement of additional mechanical



66 forces to increase the mass transfer of the pollutant to enhance removal efficiency, which limits
67 the practical implementation of adsorption materials. Recent advances in environmental
68 nanotechnology have therefore focused on decontamination using self-propelled materials
69 (Calvo-Marzal et al., 2010; Liu et al., 2010; Sánchez et al., 2015; Wang and Pumera, 2015; Chen
70 et al., 2017; Xu et al., 2017). Pt/Fe-, MnO₂-, and Ag-based materials have been widely deployed
71 as self-propelled materials in the presence of certain chemicals for water purification (Ye et al.,
72 2017; Chen et al., 2018; Lee et al., 2018; Ye et al., 2018). These materials decompose hydrogen
73 peroxide fuel (H₂O₂) and generate bubbles to move the adsorbent through the aqueous
74 environment. The bubble generating materials are therefore of considerable interest because of
75 their enhanced micro-mixing capability owing to bubble propulsion, which increases pollutant
76 transfer from the solution phase to the surface of the adsorbent and thereby improves the removal
77 of pollutants through oxidation/adsorption processes (Gao et al., 2013b; Safdar et al., 2015;
78 Vilela et al., 2016; Lee et al., 2018). However, the major difficulty in handling these adsorbents is
79 the requirement for expensive supporting metals such as Pt, Au, and Ag, which can cause toxic
80 effects when released into the aquatic system. Hence, current research is focused on
81 environmentally friendly, stable, and easily accessible materials for such applications (Chen et
82 al., 2018).

83 Metal oxide nanocomposites containing Fe₃O₄ have attracted considerable interest for
84 environmental remediation owing to their excellent magnetic and surface properties (Kim et al.,
85 2013; Kang et al., 2019). MnO₂-coated iron oxides have been demonstrated as an effective
86 material for the removal of water pollutants. Kim et al. reported that these composite materials
87 are effective for the removal of heavy metals, but require mechanical stirring (Kim et al., 2013).
88 Moreover, Kang et al. utilized the same material in advanced oxidation processes and adsorptive



89 bubble separation of various dyes in the presence of a surfactant and H₂O₂ (Kang et al., 2019).
90 These materials have also been found effective for the simultaneous removal of organics and
91 microplastics by the micro-mixing effect (Ye et al., 2021a). However, both studies used
92 surfactants for the generation of bubbles and the subsequent micro-mixing effect (Kang et al.,
93 2019; Ye et al., 2021a). Surfactants are also considered an important water pollution source all
94 over the world (Sasi et al., 2021). Therefore, for practical uses, the present study attempted to
95 utilize nanomaterials that are capable of removing both organic and inorganic contaminants from
96 aqueous bodies without the use of surfactants or other fuels.

97 Mg, one of the most abundant elements in the world, is characterized by its high reactivity
98 in water and air to form oxides and hydroxides. These reactions evolve H₂ gas to enable the
99 propulsion of particles in water. Therefore, many studies have evaluated materials such as TiO₂,
100 Au/TiO₂, Au, and Ag-doped with Mg, which are used for the removal of a variety of organic
101 pollutants (Gao et al., 2013a; Mou et al., 2013; Li et al., 2014; Vilela et al., 2017). Instead, the
102 lifetime of the H₂ generation reaction is relatively short because of the rapid corrosion reaction
103 (Mou et al., 2013). The formation of a passivation layer of the corresponding hydroxide hinders
104 the further reduction of water. Mg-based alkaline materials like MgO are considered an efficient
105 material for the remediation of pollutants through adsorption owing to their high adsorption
106 capacity (Gao et al., 2008; Yu et al., 2011; Kameda et al., 2018; Chinthala et al., 2021). The MgO
107 nanoparticles are not expensive and environmentally benign, and can hence be easily used to
108 scale up the removal process. Moreover, *in vivo* toxicity evaluations, it has shown that these
109 particles are relatively less toxic than other metal oxides (TiO₂, MnO₂, ZnO, etc.,) and also
110 biocompatible (Gao et al., 2008; Sasaki et al., 2011; Yu et al., 2011). Therefore, MgO in
111 conjunction with other materials (graphene, graphene oxide and diatomite, Fe–Co–Mn



112 nanoparticles) has been widely utilized for the removal of heavy metals and many organic
113 pollutants (Mohan et al., 2017; Rahdar et al., 2019; Liu et al., 2020; Guo and Bulin, 2021). A
114 disadvantage of this process is the required mechanical stirring and separation of the material
115 after the adsorption process. Thus, the key objective of the present study was the development of
116 a MgO-based and easily separable/recoverable material for the removal of pollutants without
117 external agitation.

118 Similar to MnO₂, MgO decomposes H₂O₂ to generate O₂ gas (Zeng et al., 2020), which is
119 assumed to be helpful in the bubble-induced mixing of the particles. Thus, the combination of
120 MgO with Fe₃O₄ nanoparticles (Fe₃O₄@MgO) was proposed as an efficient material for water
121 treatment. All the previously reported micro-mixing and bubble generating systems used
122 surfactants to induce bubble formation. In addition, they had focused on only one kind of
123 pollutants (either organic or inorganic) in their removal. In contrast to the previous reports, this
124 study tried to remove both kinds of pollutants simultaneously without the use of surfactants. In
125 short, the objectives of the present study were i) to investigate the mechanism of bubble
126 generation and the micro-mixing capacity, ii) to study the potential of Fe₃O₄@MgO
127 nanocomposite for concomitant removal of Pb²⁺ and rhodamine B dye without any mechanical
128 stirring, and iii) to evaluate the applicability of the Fe₃O₄@MgO micro-mixing system to real
129 contaminated water spiked with the selected model compounds.

130 **2. Experimental section**

131 **2.1. Materials and methods**

132 Ferric chloride (FeCl₃), magnesium chloride (MgCl₂), sodium acetate, ammonium
133 hydroxide (NH₄OH), rhodamine B (RhB), and H₂O₂ were acquired from Merck (Seoul, South



134 Korea). Lead nitrate (PbNO_3), polyethylene glycol (PEG), and cetyltrimethylammonium bromide
135 (CTAB) were purchased from Sigma-Aldrich (Seoul, South Korea). Ultrapure water with a
136 specific resistivity of $>18 \text{ M}\Omega \text{ cm}$ was prepared using a Millipore (France) system.

137 **2.2. Synthesis of $\text{Fe}_3\text{O}_4@\text{MgO}$**

138 $\text{Fe}_3\text{O}_4@\text{MgO}$ was synthesized using a two-step process as reported earlier (Peng et al.,
139 2016). First, Fe_3O_4 nanoparticles were synthesized. In this step, 5 mM of FeCl_3 was prepared in
140 ethylene glycol. Sodium acetate (3.6 g) and PEG (1.0 g) were added to the previously prepared
141 FeCl_3 solution and stirred well at $50 \text{ }^\circ\text{C}$ for approximately 30 min. The mixture was then added to
142 a 100 mL Teflon-lined autoclave and heated to $200 \text{ }^\circ\text{C}$ for approximately 8 h. The obtained black
143 product of Fe_3O_4 was allowed to reach $22\text{-}25 \text{ }^\circ\text{C}$ room temperature and was then centrifuged,
144 washed several times with ethanol, and dried in a vacuum oven at $60 \text{ }^\circ\text{C}$ for 6 h (Deng et al.,
145 2005). Approximately 0.5 g of the previously prepared Fe_3O_4 was dispersed in 100 mL of 0.025
146 M CTAB and sonicated for 30 min. The solution was then mixed with 50 mL of 0.5 M MgCl_2
147 solution by constant stirring for another 1 h. NH_4OH was then added slowly to the solution to
148 reach a temperature of $70 \text{ }^\circ\text{C}$. The solution was allowed to cool until room temperature was
149 reached. The separated particles were then washed several times with ethanol and dried at $50 \text{ }^\circ\text{C}$
150 for 6 h. The $\text{Fe}_3\text{O}_4@\text{MgO}$ nanocomposites were then obtained by the calcination of the dried
151 particles at $450 \text{ }^\circ\text{C}$ for 3 h (Peng et al., 2016).

152 **2.3. Characterization of $\text{MgO}@\text{Fe}_3\text{O}_4$**

153 The morphology and structure of the $\text{MgO}@\text{Fe}_3\text{O}_4$ nanocomposites were determined through
154 scanning electron microscopy (SEM) (JSM-7401F; JEOL, Tokyo, Japan). Energy dispersive X-
155 ray (EDX) mapping was performed to obtain the surface composition of the materials. The



156 crystalline nature of the material was obtained using an X-ray diffractometer (XRD, MXP18 HF;
157 MAC Science Co., Japan). The chemical composition of the particles was analyzed using X-ray
158 photoelectron spectroscopy (XPS, K-Alpha; Thermo Scientific, USA). The bubble formation was
159 monitored, and images were captured using an optical microscope (Olympus MX51).

160 **2.4. Batch experiment and analysis**

161 Initially, a stock solution of RhB and Pb^{2+} with a concentration of 500 mg L^{-1} was
162 prepared in deionized water. The pollutant solutions for the adsorption experiment were prepared
163 from this stock solution. To study the removal efficiency in a real system, Pb^{2+} ions were spiked
164 in real groundwater (from a rural area in South Korea) and river water (collected from Hyeongsan
165 River, South Korea). Adsorption studies were conducted in a 20 mL glass vial. The solutions (10
166 mL) containing 10 mg L^{-1} pollutants (Pb^{2+} and RhB), and H_2O_2 were first prepared in the vial. A
167 specific amount of $\text{Fe}_3\text{O}_4@\text{MgO}$ was weighed and transferred into the vial. After a predetermined
168 time interval, the materials were separated using a magnet, and approximately $200 \mu\text{L}$ of the
169 solution was pipetted out for the analysis of the remaining pollutant in the solution. The
170 reusability of the $\text{Fe}_3\text{O}_4@\text{MgO}$ nanocomposite was evaluated with the addition of 10 mg L^{-1} of
171 the selected pollutants to the magnetically separated material after 15 min of each cycle.

172 The concentration of Pb, Mg, and Fe ions after each sampling was analyzed using an
173 inductively coupled plasma–optical emission spectrometer (ICP-OES, iCAP6300; Thermo
174 Scientific). The concentration of RhB was monitored using a UV spectrophotometer at a
175 wavelength of 540 nm (Varian, Palo Alto, CA, USA). An Orion™ Versa Star advanced
176 electrochemistry meter was used to monitor the changes in pH and dissolved oxygen (DO)
177 concentrations during the reaction. The removal percentage was then calculated using the eqn. 1,



$$\% \text{ removal} = \frac{(C_0 - C_t) \times 100}{C_0} \quad (1)$$

178
179 C_0 and C_t are the concentrations of the pollutants before and after the adsorption reactions
180 in mg/L.

181 3. Results and Discussions

182 3.1. Characterization of Fe₃O₄@MgO

183 As can be seen from Figs. 1A and 1B, the Fe₃O₄@MgO nanocomposite was spherical in
184 shape. The EDX mapping showed that compared to Fe, Mg was the major contributor to the
185 surface of the material (Fig. 1C).

186

187

Fig. 1.

188

189 The diffraction peaks at 30.2°, 35.6°, 42.9°, 53.7°, 57.2°, and 62.3° could be indexed to
190 the cubic structure of Fe₃O₄; whereas those at 18.2°, 36.8°, 38.1°, 42.9°, and 62.3° represented
191 the polycrystalline cubic structure of MgO. Moreover, the lack of extra peaks or peak shifts
192 observed in the XRD spectrum confirmed that no direct interaction occurred between the core
193 Fe₃O₄ and the outer MgO layer (Peng et al., 2016). The XPS spectrum also showed the presence
194 of Fe, Mg, and O in the material (Fig. S1). The high-resolution Mg 1s and O 1s spectra of
195 Fe₃O₄@MgO are shown in Fig. 2. The deconvolution of Fe 2p spectra generated four major
196 peaks which correspond to Fe²⁺ (723.8 and 710.6 eV) and Fe³⁺ (725.3 and 711.9 eV) (Fig. S2)
197 (Grosvenor et al., 2004). Mg 1s spectra showed peaks at 1301.7 and 1304.7 for Mg(OH)₂ and
198 MgO, respectively. This was further confirmed from the corresponding O 1s peaks at 530.1 and
199 531.2 eV corresponding to the Mg oxide (Khairallah et al., 2012; Alla et al., 2016).

200
201
202
203
204
205
206
207
208
209
210
211
212
213
214
215
216
217
218
219
220
221

Fig. 2.

3.2. Bubble generation and mixing phenomena

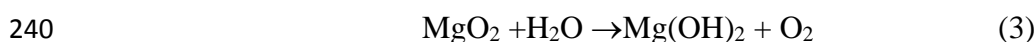
The prime objective of the study was to identify the micro-mixing phenomena by the generation of bubbles. The bubble generation was monitored without and with the addition of H₂O₂. The 1 mL of the aqueous solution containing different concentration of H₂O₂ (0%, 0.05%, 0.5%, 1%, 2%, 5%, and 10%) was put in a petri dish and 1 mg of Fe₃O₄@MgO added. The bubbles are then monitored using the optical microscope. The Fe₃O₄@MgO nanocomposites were aggregated and settled at the bottom once it was added to the aqueous solution. However, self-movement of the particles was observed with the generation of bubbles in the solution when H₂O₂ was added to the solution (Supporting Information Video S1). A small amount of surfactant (0.05%) was used to help monitor the bubble formation when using an optical microscope. The visual images of bubble formation in the solution containing Fe₃O₄@MgO with the addition of H₂O₂ are shown in Figs. 3A–C. Initially, the bubbles were generated around the material, then spread through the solution after 60 s, and finally, the entire solution was covered by the bubbles. This process continued for more than 2 min (Video S1). The bubble formation with the addition of different concentrations of H₂O₂ was monitored using an optical microscope and the results are shown in Figs. 3D–I. It can be seen from Fig. 3D that the bubbles were generated even in the presence of a low H₂O₂ concentration of 0.05% and the bubble formation and mixing of the nanocomposite in the solution increased with the increase in H₂O₂ addition. An interesting

222 observation was that the frequency of bubble generation in the medium increased until an H₂O₂
223 concentration of 5%.

224

225 **Fig. 3.**

226 The mechanism for bubble generation in Fe₃O₄@MgO in the presence of H₂O₂ can be
227 explained as follows. The reaction of H₂O₂ with MgO results in the formation of MgO₂ (Eq. 2)
228 (Zeng et al., 2020). Peroxides are well known for their oxygen generation ability when they are
229 hydrolyzed in an aqueous medium (Eq. 3). Therefore, we could not spot distinguishable peaks for
230 O 1s spectra for the corresponding peroxides (532.4 eV for Mg-O₂) (Deng et al., 2005). At the
231 same time, the high-resolution Mg 1s spectra show an increase in the peak intensity at 1301.3 eV
232 for Mg(OH)₂ after the reaction with H₂O₂. In addition, a small shift in the binding energy was also
233 observed after oxidation. Further pieces of evidence for the generation of O₂ and Mg(OH)₂ were
234 obtained by monitoring the pH and DO (Figs. 4A and B). The initial increase in DO of the
235 solution in the medium is likely owing to the oxygen formation reaction. After the reaction was
236 completed, the oxygen in the medium was removed and the DO decreased. Similarly, the pH of
237 the medium increased from the initial 4.2 to 9.0 (Fig. 4). This is an indication of Mg(OH)₂
238 formation and its release into the water.



241

242 **Fig. 4.**

243

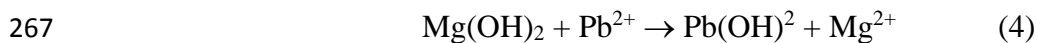
244 3.3. Applicability of the Fe₃O₄@MgO-H₂O₂ system for the removal of contaminants

245 The second objective of the study was the evaluation of the micro-mixing system in the
246 removal of water pollutants. To evaluate the applicability of the material for environmental
247 remediation purposes, both organic and inorganic contaminants were selected. The inorganic
248 contaminant described in this section was Pb²⁺ and the organic contaminant selected was a dye,
249 RhB. Fe₃O₄@MgO was added to the aqueous solution containing 10 mg L⁻¹ of pollutants (Pb²⁺
250 and RhB), with H₂O₂ (5 %). The removal efficiencies of Pb and RhB in the mixed environment
251 are shown in Fig. 5. As shown by the results of this study, nearly 100% of the initial Pb²⁺ and
252 RhB were removed from the solution after 2 h. In particular, the removal of Pb²⁺ was rapid in the
253 initial stage of the process and slowed down after 30 min, likely owing to the competition for the
254 adsorption sites with RhB.

255
256 **Fig. 5.**

257 To better understand the mechanism of heavy metal removal, further investigation was
258 performed with Pb²⁺. Using ICP-OES, a constant release of Mg²⁺ to the solution was observed
259 during the process of Pb removal (Fig. 6A). This indicates that the major mechanism for the
260 removal of heavy metals would be the cation exchange process (Cao et al., 2012); the Mg²⁺ ions
261 on the surface of the material are replaced with the positively charged heavy metal ions. As
262 described in the previous section, the surface of the material is covered with Mg(OH)₂ and can
263 react with the heavy metal ions to form Pb(OH)₂ with the release of Mg²⁺ to the solution (Eq. 4).
264 The formation of Pb(OH)₂ on the surface of the material after Pb adsorption was confirmed by
265 XPS analysis (Fig. 6B). The Pb 4f peaks located at 137.5 and 142.3 eV represent the lead oxides
266 formed by the cation exchange process (Lai et al., 2019).





268

269

270

Fig. 6.

271

272

273

274

275

276

277

278

279

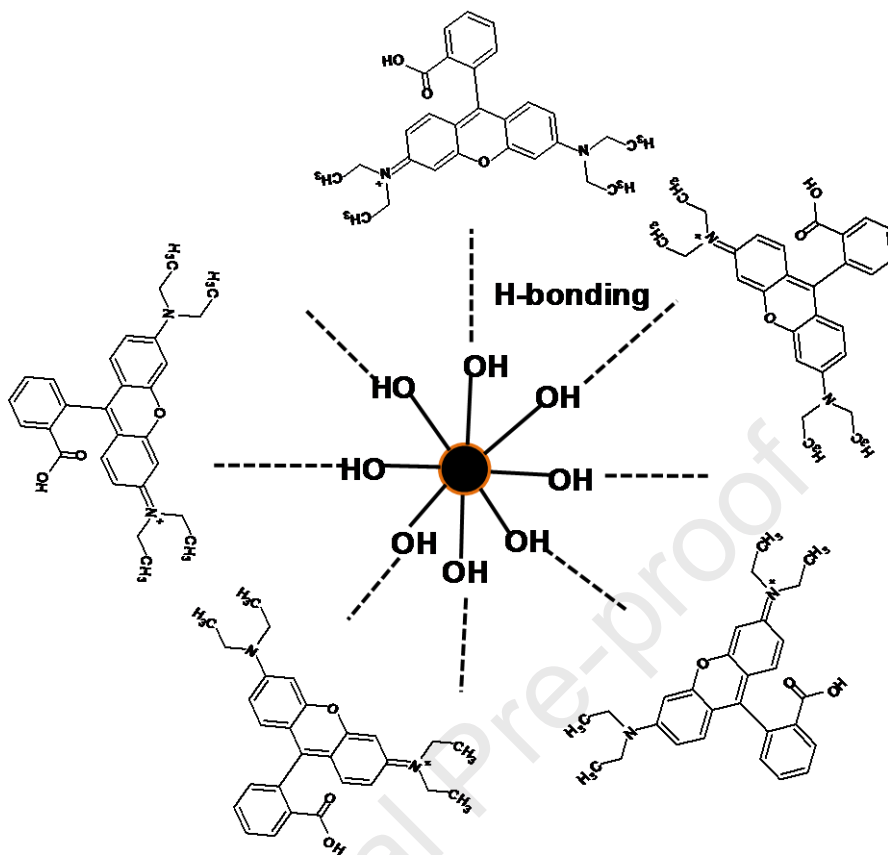
280

281

282

The organic dye removal process follows two possible mechanisms, either through the Fenton oxidation by released Fe^{2+} or by the adsorption on the surface of the nanocomposite. As Fe_3O_4 is present in the core, its direct reaction with H_2O_2 (Fenton reaction) to generate reactive oxygen species is unlikely. To confirm this, the Fe concentration leached into the solution was monitored and a very small concentration of 0.6 mg L^{-1} of Fe was detected (Fig. S3). The homogeneous Fenton reactions with this particular Fe and Mg concentration show that the removal of RhB was insignificant (Fig. S4). Therefore, the removal of RhB is mainly through physical adsorption. As described in Eqs. 2 and 3, the first step is the formation of Mg(OH)_2 . As reported for similar adsorbents, the hydrogen bonding between $-\text{OH}$ present in the Mg(OH)_2 and nitrogen in the dye molecule favors the adsorptive removal of these types of dyes (Scheme 1) (Lin and Wang, 2009).





283

284 **Scheme 1:** Mechanism for the adsorptive removal of RhB in the $\text{Fe}_3\text{O}_4@\text{MgO}-\text{H}_2\text{O}_2$ system

285

286

287 3.4. Effects of operational parameters

288 The removal efficiency of the process depends on various factors such as concentrations
 289 of $\text{Fe}_3\text{O}_4@\text{MgO}$, H_2O_2 , and the initial pH. Hence, to obtain a better performance of the system,
 290 the removal efficiency was evaluated at varying concentrations of the nanomaterial and H_2O_2 and
 291 pH. The results of Pb^{2+} removal under varying operating conditions are presented in Fig. 7 and
 292 that of RhB are shown in Supporting Information (Fig. S5).

293 *Effect of H_2O_2 concentration*



294 The H_2O_2 concentration (0–10%) influenced the adsorption of Pb^{2+} (10 ppm) at a fixed
295 $\text{Fe}_3\text{O}_4@\text{MgO}$ dose (0.8 g L^{-1}) (Fig. 7A). The removal efficiency of 20% was observed without
296 the addition of H_2O_2 , and the removal efficiency increased with the increase of reaction time.
297 Interestingly, it is clear from Fig. 3H that even a small addition of H_2O_2 (0.5%) resulted in 34%
298 Pb removal after 15 min which increased to 89% after 60 min. When the concentration of H_2O_2
299 increased to 5% and 10%, more than 90% removal was attained within a short period of 15 min.
300 Instead, for RhB, the removal was negligible in the presence of $\text{Fe}_3\text{O}_4@\text{MgO}$ without H_2O_2 .
301 However, the removal of RhB increased to 75%, 85%, and 100% with the increase in H_2O_2
302 concentrations to 0.5%, 1%, and 10%, respectively.

303 It is clear from the XPS analysis that in the absence of H_2O_2 , the adsorbent layer exists as
304 MgO. Consequently, there will not be any bubble formation and thus, the system remains
305 immobile. This implies that the bubble formation and subsequent mixing effect have a prominent
306 role in the removal of pollutants. Moreover, when the concentration of H_2O_2 increased, the
307 material started moving through the solution to capture Pb^{2+} ions along with the generation of
308 bubbles.

309 ***Effect of $\text{Fe}_3\text{O}_4@\text{MgO}$***

310 The effect of $\text{Fe}_3\text{O}_4@\text{MgO}$ concentration ($0.2\text{--}1 \text{ g L}^{-1}$) was evaluated at a fixed H_2O_2
311 concentration of 5% (Fig. 7B). A clear difference in the removal efficiency was observed during
312 the initial period. Removal efficiencies of 0%, 46%, 63%, 80%, and 81% were observed with 0,
313 0.2, 0.4, 0.8, and 1 g L^{-1} of $\text{Fe}_3\text{O}_4@\text{MgO}$, respectively. A similar removal pattern was observed
314 for RhB. This difference could be correlated with the lack of adsorption sites at a low dose of the
315 material. The adsorption sites increased with the increase in adsorbent concentration and reaction
316 with H_2O_2 .



317 *Effect of pH*

318 pH is another important parameter in the remediation process, and therefore experiments
319 were conducted at different initial pHs such as 2, 5, 7.5, 9, and 11 with the optimized condition of
320 H₂O₂ concentration of 5% and Fe₃O₄@MgO dose of 0.8 g L⁻¹. As in the previous cases, a
321 noticeable effect was observed at the initial time of 15 min. The removal efficiencies were 62%,
322 63%, 85%, 84%, and 83% at pH 2, 5, 7.5, 9, and 11, respectively for Pb²⁺ ion removal (Fig. 7C).
323 However, for RhB, removal efficiencies of 53%, 63%, 62%, 68%, and 89% were observed after
324 45 min at these pHs.

325 Since the isoelectric point of MgO is 11, the difference in the adsorption could not be
326 discussed in relation to the material property (Wang et al., 2017). Therefore, the removal
327 efficiencies under varying pH could be due to the different speciation of Pb²⁺. The Pb species
328 exist as Pb²⁺, Pb(OH)⁺, Pb(OH)₂⁰, and Pb(OH)₃⁻ at pH < 6, 8, > 9, and > 12, respectively (Sheng
329 et al., 2009; Mohan et al., 2017). When the pH is less than 6, the major species is Pb²⁺, and the
330 competitive adsorption between H⁺ and Pb²⁺ on the surface of the material leads to a low
331 adsorption capacity. Likewise, when the pH increases the precipitation of hydroxides occurs to
332 enhance the removal efficiency. This is further supported by the lower solubility product of
333 Pb(OH)₂ ($k_{sp} = 1.43 \times 10^{-20}$) than that of Mg(OH)₂ (5.61×10^{-12}) (Ponomarev et al., 2019).
334 Moreover, the electrostatic repulsion of RhB from the MgO surface at acidic pH results in
335 reduced removal. Similarly, electrostatic attraction between the positively charged RhB and the
336 negatively charged Fe₃O₄@MgO should enhance their removal at high pH (Liu et al., 2020).

337
338
339 **Fig. 7.**



340 **3.5. Evaluation of Fe₃O₄@MgO-H₂O₂ practical application**

341 To attain our third objective, the performance of the Fe₃O₄@MgO-H₂O₂ particles under
342 environmentally relevant conditions, some supplementary experiments such as reusability,
343 removal of other heavy metals, and removal efficiency in real groundwater (from a rural area in
344 South Korea) and river water (collected from Hyeongsan River, South Korea) spiked with Pb²⁺
345 were studied. The physicochemical characteristics of the ground and river water are listed in
346 Supporting Information (Table S1).

347 The results of the reusability test are shown in Supporting Information (Fig. S6). It was
348 found that more than 90% of the initial Pb was removed in the first cycle, and subsequently, the
349 adsorption capacity was reduced. This is likely due to the leaching of Mg ions from the surface of
350 MgO@Fe₃O₄. In addition, the capacity of MgO@Fe₃O₄ for other heavy metals such as Cd, Ni,
351 Zn, Co, and Cu was also investigated and the results are shown in Fig. 8A. As shown by the
352 results, all the selected heavy metals could be removed effectively by the MgO@Fe₃O₄-H₂O₂
353 system. The experiments with ground and river water spiked with Pb²⁺ showed that there was no
354 significant difference in the removal efficiencies between them even when they contained
355 different co-existing or interfering ions (Fig. 8B), showing good environmental adaptation
356 capability of the system.

359 **Fig. 8.**

360 The Fe₃O₄@MgO nanocomposite-H₂O₂ system possessed several advantages over other
361 similar systems (Fe₃O₄@MnO₂-H₂O₂) (Kang et al., 2019; Ye et al., 2021a), the MgO based
362 nanocomposites (Mohan et al., 2017; Rahdar et al., 2019; Liu et al., 2020; Guo and Bulin, 2021).

363 In contrast to other MgO-based materials and other adsorbents, the present system allowed
364 superior activity for the removal of heavy metals concomitant with dyes without any external
365 shaking. Most importantly, in comparison with the other micro-mixing systems, the present study
366 doesn't require surfactants. We anticipate that the findings presented in this study will offer a
367 promising strategy for the on-site removal of a variety of pollutants from contaminated water.
368 Furthermore, it is proposed that the Fe₃O₄@MgO nanocomposite could be used along with other
369 oxidants such as persulfate and ozone to induce the oxidation of pollutants. The increase of pH
370 with the addition of Fe₃O₄@MgO to the aqueous solution will be beneficial for ozone activation.
371 In the same way, polymeric membranes could also be fabricated with Fe₃O₄@MgO for water
372 purification and other environmental applications.

373

374 **4. Conclusions**

375 We have verified that the Fe₃O₄@MgO nanocomposite is very effective in the generation of
376 bubbles in the presence of H₂O₂. As a result, the generation of oxygen bubbles in the presence of
377 H₂O₂ promoted the agitation of the solution containing Fe₃O₄@MgO. The bubble generation and
378 the following self-mixing mechanism enhanced the simultaneous removal of both Pb²⁺ and
379 rhodamine B with exceptional stability. The effect of H₂O₂ concentration and initial pH revealed
380 that the adsorption was induced at a low H₂O₂ concentration of 0.05% and is effective over a
381 wide pH range (2.5 to 11). The data obtained from the XPS and ICP-OES analyses showed that
382 the adsorption of Pb²⁺ occurred via the cation exchange mechanism. The unfeasibility of the
383 homogeneous Fenton reaction in this system showed that adsorption by Fe₃O₄@MgO is the
384 predominant mechanism for the removal of RhB. The nearly similar removal efficiencies in pure,
385 river, and groundwater matrices and for different heavy metals is an important advantage. Thus,



386 Fe₃O₄@MgO could be proposed as an efficient adsorbent for the removal of a variety of water
387 contaminants from their sources.

388 **Conflicts of interest**

389 There are no conflicts to declare

390 **Acknowledgment**

391 This research was supported by the National Research Foundation of Korea (NRF) grant funded
392 by the Korean government (MEST) (No. 2017R1A2B3012681).

393

394 **References**

395 Abdullah, N., Yusof, N., Lau, W.J., Jaafar, J., Ismail, A.F., 2019. Recent trends of heavy metal
396 removal from water/wastewater by membrane technologies. *Journal of Industrial and Engineering*
397 *Chemistry* 76, 17-38.

398 Afroze, S., Sen, T.K., 2018. A Review on Heavy Metal Ions and Dye Adsorption from Water by
399 Agricultural Solid Waste Adsorbents. *Water, Air, & Soil Pollution* 229, 225.

400 Alla, S.K., Verma, A.D., Kumar, V., Mandal, R.K., Sinha, I., Prasad, N.K., 2016. Solvothermal
401 synthesis of CuO–MgO nanocomposite particles and their catalytic applications. *RSC Advances*
402 6, 61927-61933.

403 Calvo-Marzal, P., Sattayasamitsathit, S., Balasubramanian, S., Windmiller, J.R., Dao, C., Wang,
404 J., 2010. Propulsion of nanowire diodes. *Chemical Communications* 46, 1623-1624.

405 Cao, C.-Y., Qu, J., Wei, F., Liu, H., Song, W.-G., 2012. Superb Adsorption Capacity and
406 Mechanism of Flowerlike Magnesium Oxide Nanostructures for Lead and Cadmium Ions. *ACS*
407 *Applied Materials & Interfaces* 4, 4283-4287.



408 Castro-Muñoz, R., González-Melgoza, L.L., García-Depraect, O., 2021. Ongoing progress on
409 novel nanocomposite membranes for the separation of heavy metals from contaminated water.
410 *Chemosphere* 270, 129421.

411 Chen, C., Karshalev, E., Guan, J., Wang, J., 2018. Magnesium-Based Micromotors: Water-
412 Powered Propulsion, Multifunctionality, and Biomedical and Environmental Applications. *Small*
413 14, 1704252.

414 Chen, C.C., Chaudhary, A.J., Grimes, S.M., 2007. The effect of sodium hydroxide in photolytic
415 and photocatalytic degradation of Acid Blue 29 and Ethyl Violet. *Dyes and Pigments* 73, 55-58.

416 Chen, X.-Z., Hoop, M., Mushtaq, F., Siringil, E., Hu, C., Nelson, B.J., Pané, S., 2017. Recent
417 developments in magnetically driven micro- and nanorobots. *Applied Materials Today* 9, 37-48.

418 Chinthala, M., Balakrishnan, A., Venkataraman, P., Manaswini Gowtham, V., Polagani, R.K.,
419 2021. Synthesis and applications of nano-MgO and composites for medicine, energy, and
420 environmental remediation: a review. *Environmental Chemistry Letters* 19, 4415-4454.

421 Deng, H., Li, X., Peng, Q., Wang, X., Chen, J., Li, Y., 2005. Monodisperse Magnetic Single-
422 Crystal Ferrite Microspheres. *Angewandte Chemie International Edition* 44, 2782-2785.

423 Dotto, J., Fagundes-Klen, M.R., Veit, M.T., Palácio, S.M., Bergamasco, R., 2019. Performance
424 of different coagulants in the coagulation/flocculation process of textile wastewater. *Journal of*
425 *Cleaner Production* 208, 656-665.

426 Gao, C., Zhang, W., Li, H., Lang, L., Xu, Z., 2008. Controllable Fabrication of Mesoporous MgO
427 with Various Morphologies and Their Absorption Performance for Toxic Pollutants in Water.
428 *Crystal Growth & Design* 8, 3785-3790.

429 Gao, W., Feng, X., Pei, A., Gu, Y., Li, J., Wang, J., 2013a. Seawater-driven magnesium based
430 Janus micromotors for environmental remediation. *Nanoscale* 5, 4696-4700.



431 Gao, W., Sattayasamitsathit, S., Orozco, J., Wang, J., 2013b. Efficient bubble propulsion of
432 polymer-based microengines in real-life environments. *Nanoscale* 5, 8909-8914.

433 Ghaedi, S., Seifpanahi-Shabani, K., Sillanpää, M., 2022. Waste-to-Resource: New application of
434 modified mine silicate waste to remove Pb²⁺ ion and methylene blue dye, adsorption properties,
435 mechanism of action and recycling. *Chemosphere* 292, 133412.

436 Grosvenor, A.P., Kobe, B.A., Biesinger, M.C., McIntyre, N.S., 2004. Investigation of multiplet
437 splitting of Fe 2p XPS spectra and bonding in iron compounds. *Surface and Interface Analysis*
438 36, 1564-1574.

439 Guo, T., Bulin, C., 2021. Facile preparation of MgO/graphene oxide nanocomposite for efficient
440 removal of aqueous Congo red: adsorption performance and interaction mechanism. *Research on*
441 *Chemical Intermediates* 47, 945-971.

442 Iqbal, J., Shah, N.S., Sayed, M., Niazi, N.K., Imran, M., Khan, J.A., Khan, Z.U.H., Hussien,
443 A.G.S., Polychronopoulou, K., Howari, F., 2021. Nano-zerovalent manganese/biochar composite
444 for the adsorptive and oxidative removal of Congo-red dye from aqueous solutions. *Journal of*
445 *Hazardous Materials* 403, 123854.

446 Joseph, L., Jun, B.-M., Flora, J.R.V., Park, C.M., Yoon, Y., 2019. Removal of heavy metals from
447 water sources in the developing world using low-cost materials: A review. *Chemosphere* 229,
448 142-159.

449 Kameda, K., Hashimoto, Y., Ok, Y.S., 2018. Stabilization of arsenic and lead by magnesium
450 oxide (MgO) in different seawater concentrations. *Environmental Pollution* 233, 952-959.

451 Kang, Y.-G., Yoon, H., Lee, C.-S., Kim, E.-J., Chang, Y.-S., 2019. Advanced oxidation and
452 adsorptive bubble separation of dyes using MnO₂-coated Fe₃O₄ nanocomposite. *Water Research*
453 151, 413-422.



454 Khairallah, F., Glisenti, A., Natile, M.M., Galenda, A., 2012. CuO/MgO Nanocomposites by Wet
455 Impregnation: An XPS Study. *Surface Science Spectra* 19, 23-29.

456 Kim, E.-J., Lee, C.-S., Chang, Y.-Y., Chang, Y.-S., 2013. Hierarchically Structured Manganese
457 Oxide-Coated Magnetic Nanocomposites for the Efficient Removal of Heavy Metal Ions from
458 Aqueous Systems. *ACS Applied Materials & Interfaces* 5, 9628-9634.

459 Kim, S., Park, C.M., Jang, M., Son, A., Her, N., Yu, M., Snyder, S., Kim, D.-H., Yoon, Y., 2018.
460 Aqueous removal of inorganic and organic contaminants by graphene-based nanoadsorbents: A
461 review. *Chemosphere* 212, 1104-1124.

462 Lai, H., Deng, J., Wen, S., Liu, Q., 2019. Elucidation of lead ions adsorption mechanism on
463 marmatite surface by PCA-assisted ToF-SIMS, XPS and zeta potential. *Minerals Engineering*
464 144, 106035.

465 Lee, C.-S., Gong, J., Oh, D.-S., Jeon, J.-R., Chang, Y.-S., 2018. Zerovalent-Iron/Platinum Janus
466 Micromotors with Spatially Separated Functionalities for Efficient Water Decontamination. *ACS*
467 *Applied Nano Materials* 1, 768-776.

468 Li, J., Singh, V.V., Sattayasamitsathit, S., Orozco, J., Kaufmann, K., Dong, R., Gao, W., Jurado-
469 Sanchez, B., Fedorak, Y., Wang, J., 2014. Water-Driven Micromotors for Rapid Photocatalytic
470 Degradation of Biological and Chemical Warfare Agents. *ACS Nano* 8, 11118-11125.

471 Lin, J.X., Wang, L., 2009. Adsorption of dyes using magnesium hydroxide-modified diatomite.
472 *Desalination and Water Treatment* 8, 263-271.

473 Liu, M., Zentgraf, T., Liu, Y., Bartal, G., Zhang, X., 2010. Light-driven nanoscale plasmonic
474 motors. *Nature Nanotechnology* 5, 570-573.



475 Liu, N., Wu, Y., Sha, H., 2020. Magnesium oxide modified diatomite waste as an efficient
476 adsorbent for organic dye removal: adsorption performance and mechanism studies. *Separation*
477 *Science and Technology* 55, 234-246.

478 Malik, V., Saya, L., Gautam, D., Sachdeva, S., Dheer, N., Arya, D.K., Gambhir, G., Hooda, S.,
479 2022. Review on adsorptive removal of metal ions and dyes from wastewater using tamarind-
480 based bio-composites. *Polymer Bulletin*.

481 Mohan, S., Kumar, V., Singh, D.K., Hasan, S.H., 2017. Effective removal of lead ions using
482 graphene oxide-MgO nanohybrid from aqueous solution: Isotherm, kinetic and thermodynamic
483 modeling of adsorption. *Journal of Environmental Chemical Engineering* 5, 2259-2273.

484 Mou, F., Chen, C., Ma, H., Yin, Y., Wu, Q., Guan, J., 2013. Self-Propelled Micromotors Driven
485 by the Magnesium–Water Reaction and Their Hemolytic Properties. *Angewandte Chemie*
486 *International Edition* 52, 7208-7212.

487 Nadeem, M., Mahmood, A., Shahid, S.A., Shah, S.S., Khalid, A.M., McKay, G., 2006. Sorption
488 of lead from aqueous solution by chemically modified carbon adsorbents. *Journal of Hazardous*
489 *Materials* 138, 604-613.

490 Nigam, P., Banat, I.M., Singh, D., Marchant, R., 1996. Microbial process for the decolorization
491 of textile effluent containing azo, diazo and reactive dyes. *Process Biochemistry* 31, 435-442.

492 Osagie, C., Othmani, A., Ghosh, S., Malloum, A., Kashitarash Esfahani, Z., Ahmadi, S., 2021.
493 Dyes adsorption from aqueous media through the nanotechnology: A review. *Journal of Materials*
494 *Research and Technology* 14, 2195-2218.

495 Peng, H., Wang, X., Hu, C., Hu, J., Tian, X., 2016. A simple approach for the synthesis of bi-
496 functional Fe₃O₄@MgO core–shell nanoparticles with magnetic-microwave to heat responsive
497 properties. *New Journal of Chemistry* 40, 7911-7916.



498 Ponomarev, N., Pastushok, O., Repo, E., Doshi, B., Sillanpää, M., 2019. Lignin-Based
499 Magnesium Hydroxide Nanocomposite. Synthesis and Application for the Removal of Potentially
500 Toxic Metals from Aqueous Solution. *ACS Applied Nano Materials* 2, 5492-5503.

501 Qiu, B., Tao, X., Wang, H., Li, W., Ding, X., Chu, H., 2021. Biochar as a low-cost adsorbent for
502 aqueous heavy metal removal: A review. *Journal of Analytical and Applied Pyrolysis* 155,
503 105081.

504 Rahdar, S., Rahdar, A., Zafar, M.N., Shafqat, S.S., Ahmadi, S., 2019. Synthesis and
505 characterization of MgO supported Fe–Co–Mn nanoparticles with exceptionally high adsorption
506 capacity for Rhodamine B dye. *Journal of Materials Research and Technology* 8, 3800-3810.

507 Rasaki, S.A., Bingxue, Z., Guarecuco, R., Thomas, T., Minghui, Y., 2019. Geopolymer for use in
508 heavy metals adsorption, and advanced oxidative processes: A critical review. *Journal of Cleaner*
509 *Production* 213, 42-58.

510 Safdar, M., Wani, O.M., Jänis, J., 2015. Manganese Oxide-Based Chemically Powered
511 Micromotors. *ACS Applied Materials & Interfaces* 7, 25580-25585.

512 Sánchez, S., Soler, L., Katuri, J., 2015. Chemically Powered Micro- and Nanomotors.
513 *Angewandte Chemie International Edition* 54, 1414-1444.

514 Sasaki, K., Fukumoto, N., Moriyama, S., Hirajima, T., 2011. Sorption characteristics of fluoride
515 on to magnesium oxide-rich phases calcined at different temperatures. *Journal of Hazardous*
516 *Materials* 191, 240-248.

517 Sasi, S., Rayaroth, M.P., Aravindakumar, C.T., Aravind, U.K., 2021. Alcohol ethoxysulfates
518 (AES) in environmental matrices. *Environmental Science and Pollution Research* 28, 34167-
519 34186.



520 Sheng, G., Wang, S., Hu, J., Lu, Y., Li, J., Dong, Y., Wang, X., 2009. Adsorption of Pb(II) on
521 diatomite as affected via aqueous solution chemistry and temperature. *Colloids and Surfaces A:
522 Physicochemical and Engineering Aspects* 339, 159-166.

523 Vakili, M., Rafatullah, M., Ibrahim, M.H., Abdullah, A.Z., Salamatinia, B., Gholami, Z., 2014.
524 Oil Palm Biomass as an Adsorbent for Heavy Metals. in: Whitacre, D.M. (Ed.). *Reviews of
525 Environmental Contamination and Toxicology* Volume 232. Springer International Publishing,
526 Cham, pp. 61-88.

527 Valix, M., Cheung, W.H., McKay, G., 2004. Preparation of activated carbon using low
528 temperature carbonisation and physical activation of high ash raw bagasse for acid dye
529 adsorption. *Chemosphere* 56, 493-501.

530 Vilela, D., Parmar, J., Zeng, Y., Zhao, Y., Sánchez, S., 2016. Graphene-Based Microbots for
531 Toxic Heavy Metal Removal and Recovery from Water. *Nano Letters* 16, 2860-2866.

532 Vilela, D., Stanton, M.M., Parmar, J., Sánchez, S., 2017. Microbots Decorated with Silver
533 Nanoparticles Kill Bacteria in Aqueous Media. *ACS Applied Materials & Interfaces* 9, 22093-
534 22100.

535 Wang, B., Xiong, X., Ren, H., Huang, Z., 2017. Preparation of MgO nanocrystals and catalytic
536 mechanism on phenol ozonation. *RSC Advances* 7, 43464-43473.

537 Wang, H., Pumera, M., 2015. Fabrication of Micro/Nanoscale Motors. *Chemical Reviews* 115,
538 8704-8735.

539 Xu, T., Xu, L.-P., Zhang, X., 2017. Ultrasound propulsion of micro-/nanomotors. *Applied
540 Materials Today* 9, 493-503.

541 Ye, H., Kang, J., Ma, G., Sun, H., Wang, S., 2018. High-speed graphene@Ag-MnO₂
542 micromotors at low peroxide levels. *Journal of Colloid and Interface Science* 528, 271-280.



543 Ye, H., Sun, H., Wang, S., 2017. Electrochemical synthesis of graphene/MnO₂ in an architecture
544 of bilayer microtubes as micromotors. *Chemical Engineering Journal* 324, 251-258.

545 Ye, H., Wang, Y., Liu, X., Xu, D., Yuan, H., Sun, H., Wang, S., Ma, X., 2021a. Magnetically
546 steerable iron oxides-manganese dioxide core-shell micromotors for organic and microplastic
547 removals. *Journal of Colloid and Interface Science* 588, 510-521.

548 Ye, S., Chen, Y., Yao, X., Zhang, J., 2021b. Simultaneous removal of organic pollutants and
549 heavy metals in wastewater by photoelectrocatalysis: A review. *Chemosphere* 273, 128503.

550 Yu, X.-Y., Luo, T., Jia, Y., Zhang, Y.-X., Liu, J.-H., Huang, X.-J., 2011. Porous Hierarchically
551 Micro-/Nanostructured MgO: Morphology Control and Their Excellent Performance in As(III)
552 and As(V) Removal. *The Journal of Physical Chemistry C* 115, 22242-22250.

553 Zazou, H., Afanga, H., Akhouairi, S., Ouchtak, H., Addi, A.A., Akbour, R.A., Assabbane, A.,
554 Douch, J., Elmchaouri, A., Duplay, J., Jada, A., Hamdani, M., 2019. Treatment of textile industry
555 wastewater by electrocoagulation coupled with electrochemical advanced oxidation process.
556 *Journal of Water Process Engineering* 28, 214-221.

557 Zeng, W., Yin, Z., Gao, M., Wang, X., Feng, J., Ren, Y., Wei, T., Fan, Z., 2020. In-situ growth of
558 magnesium peroxide on the edge of magnesium oxide nanosheets: Ultrahigh photocatalytic
559 efficiency based on synergistic catalysis. *Journal of Colloid and Interface Science* 561, 257-264.

560

561



Figure captions

562
563
564 **Fig. 1.** Scanning electron microscopy images (A and B), energy dispersive X-ray spectra (C), and
565 X-ray diffraction pattern (D) of Fe₃O₄@MgO nanocomposites.

566
567 **Fig. 2.** Mg 1s X-ray photoelectron spectroscopy (XPS) spectra (A and C) and O 1s XPS spectra
568 (B and D) of Fe₃O₄@MgO before and after H₂O₂ treatment.

569
570 **Fig. 3.** Photographic images of bubble formation with the addition of Fe₃O₄@MgO in the
571 solution containing H₂O₂; 1 s (A), 60 s (B), and 90 s (C). Microscopic images (scale bar 10 μm)
572 of bubble generation with the addition of 0.05% (D), 0.5% (E), 1% (F), 2% (G), 5% (H), and
573 10% (I) H₂O₂.

574
575 **Fig. 4.** Time-dependent changes in the pH (A) and dissolved oxygen (DO) (B) of deionized water
576 in the Fe₃O₄@MgO-H₂O₂ system. Experimental conditions: [Fe₃O₄@MgO] = 0.8 g/L, [H₂O₂] =
577 5%.

578
579 **Fig. 5.** Simultaneous removal of Pb²⁺ and RhB by Fe₃O₄@MgO with the addition of H₂O₂.
580 Experimental conditions: [Fe₃O₄@MgO] = 0.8 g L⁻¹, [H₂O₂] = 5%, and [Pollutants] = 10 mg L⁻¹.

581
582 **Fig. 6.** Time-dependent release of Mg²⁺ ions from Fe₃O₄@MgO during the adsorption reaction
583 (A) and X-ray photoelectron spectroscopy of Pb 4f spectra of Fe₃O₄@MgO particles after the



584 adsorption of Pb^{2+} (B). Experimental conditions: $[\text{Fe}_3\text{O}_4@\text{MgO}] = 0.8 \text{ g L}^{-1}$, $[\text{H}_2\text{O}_2] = 5\%$, and
585 $[\text{Pb}^{2+}] = 10 \text{ mg L}^{-1}$.

586
587 **Fig. 7.** Effect of H_2O_2 (A), TX-100 (B), $\text{Fe}_3\text{O}_4@\text{MgO}$ dose (C), and pH (D) on the removal of
588 Pb^{2+} in the $\text{Fe}_3\text{O}_4@\text{MgO}-\text{H}_2\text{O}_2$ system. Experimental conditions: $[\text{Pb}^{2+}] = 10 \text{ mg L}^{-1}$.

589
590 **Fig. 8.** Removal of Pb^{2+} from deionized, ground, and river water (A) and removal efficiency of
591 various heavy metals (B) by the $\text{Fe}_3\text{O}_4@\text{MgO}-\text{H}_2\text{O}_2$ system. Experimental conditions:
592 $[\text{Fe}_3\text{O}_4@\text{MgO}] = 0.8 \text{ g L}^{-1}$, $[\text{H}_2\text{O}_2] = 5\%$, $[\text{Pb}^{2+}] = 10 \text{ mg L}^{-1}$, and pH 7.5

593

Journal Pre-proof



Figures

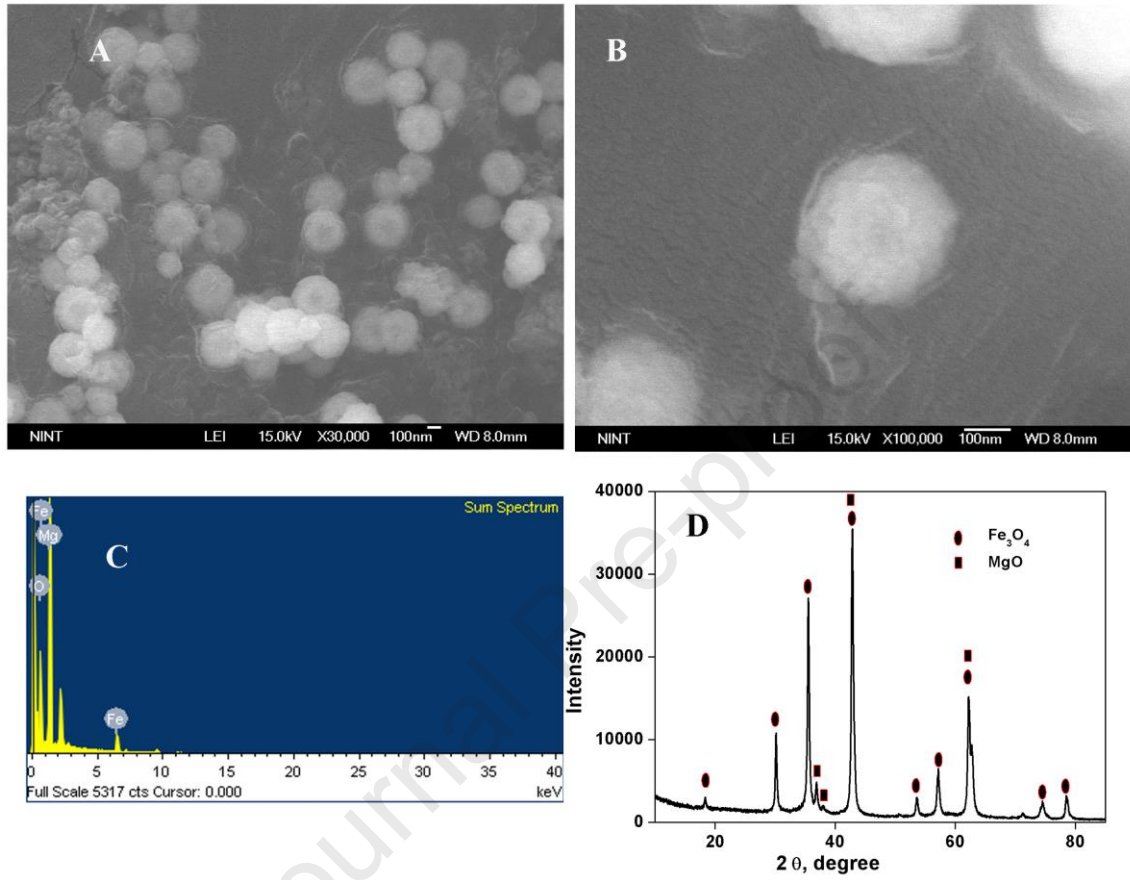


Fig. 1

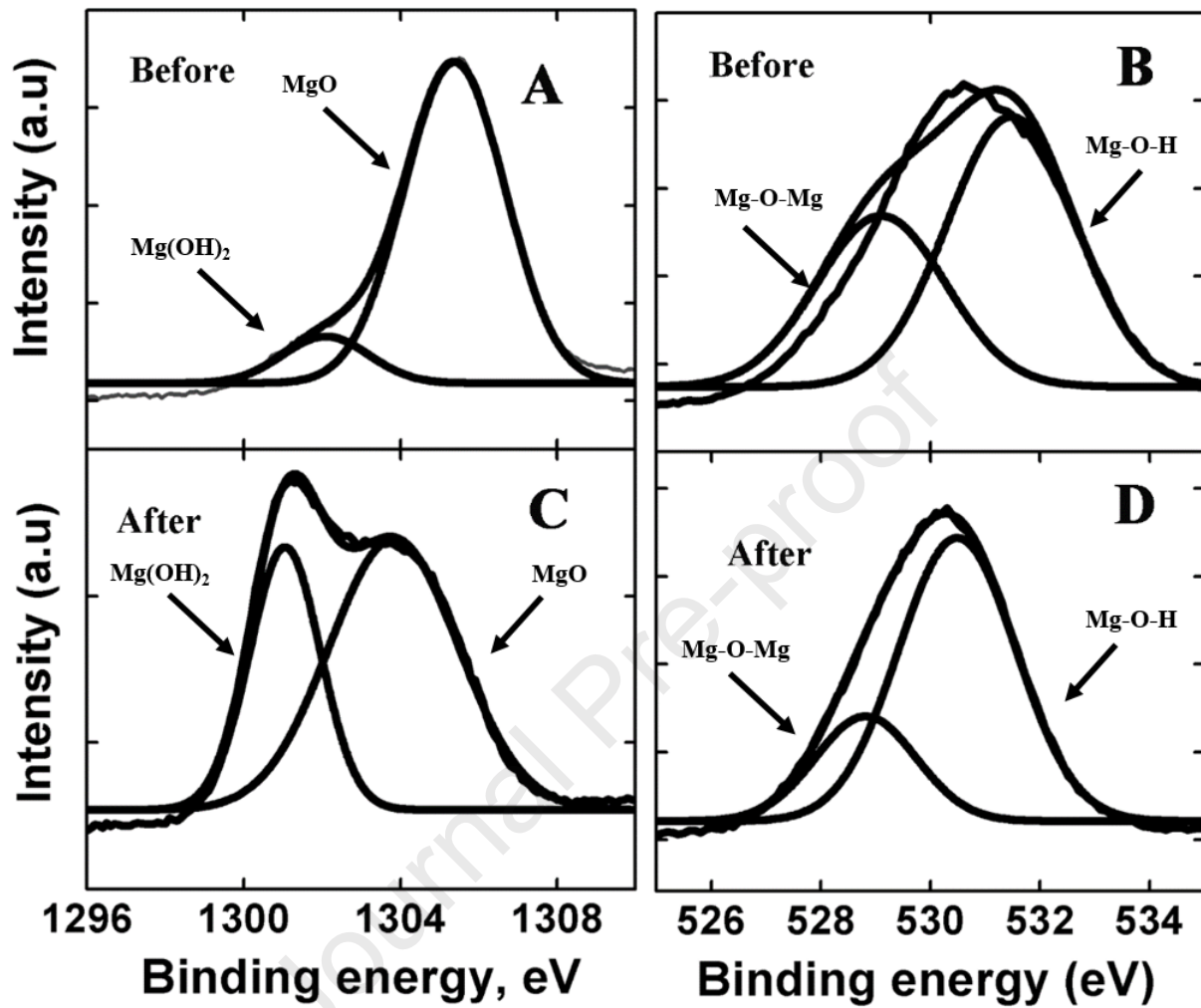


Fig. 2

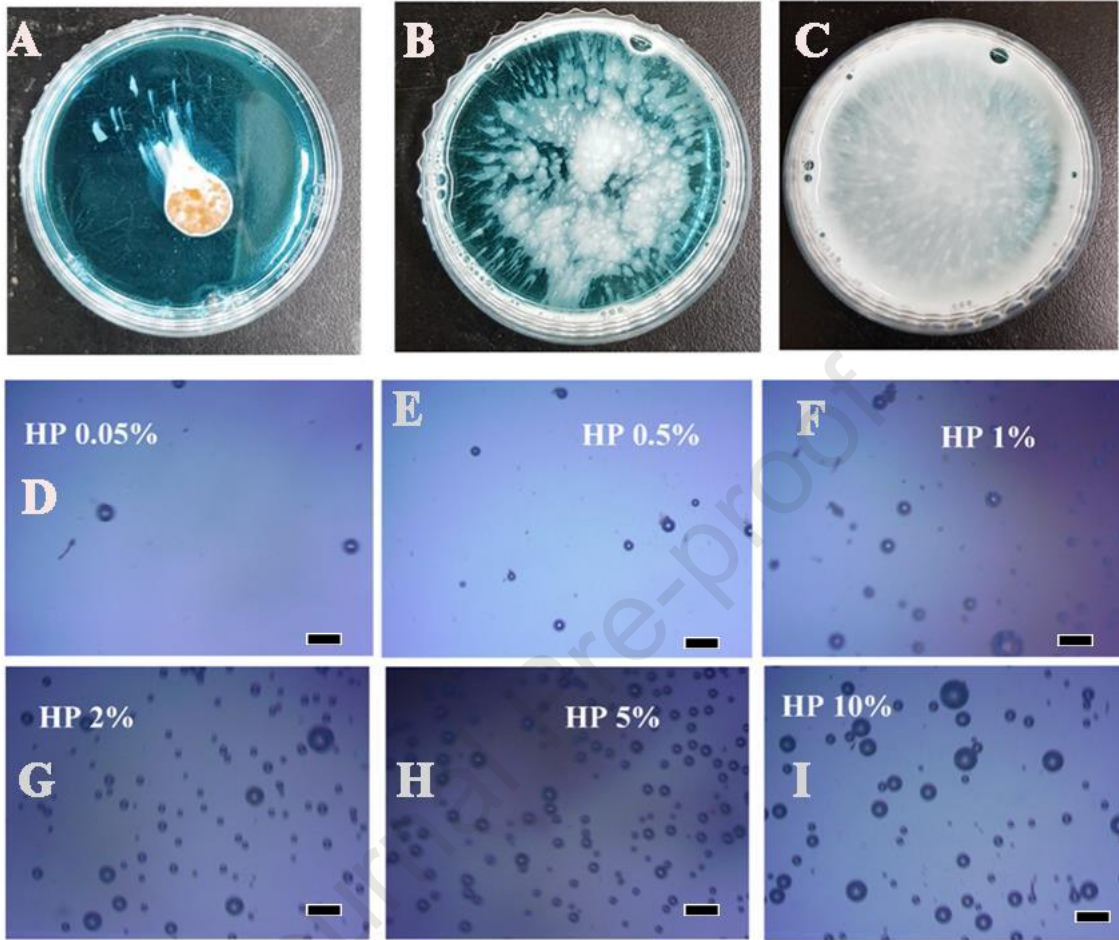


Fig. 3

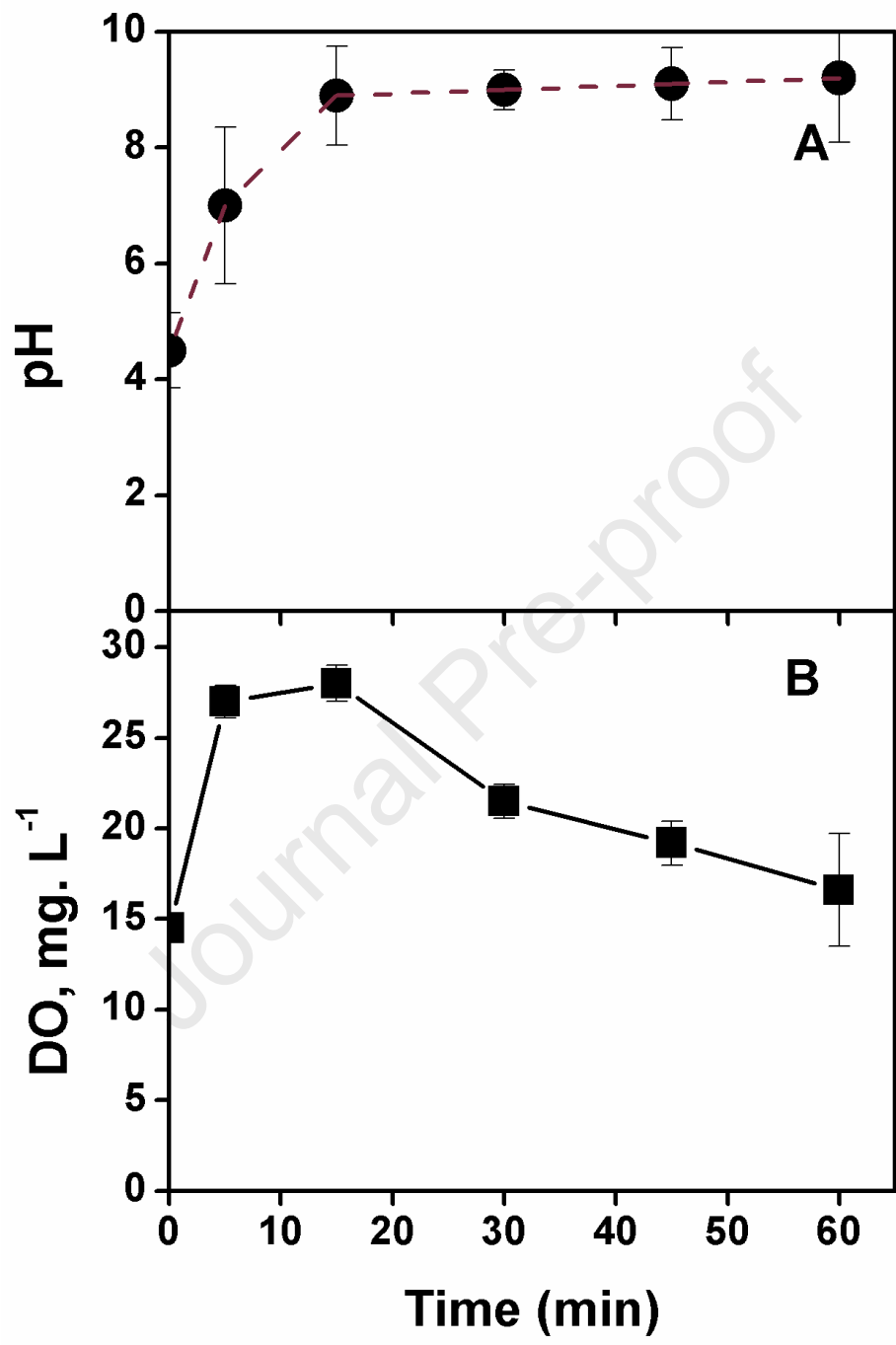


Fig. 4

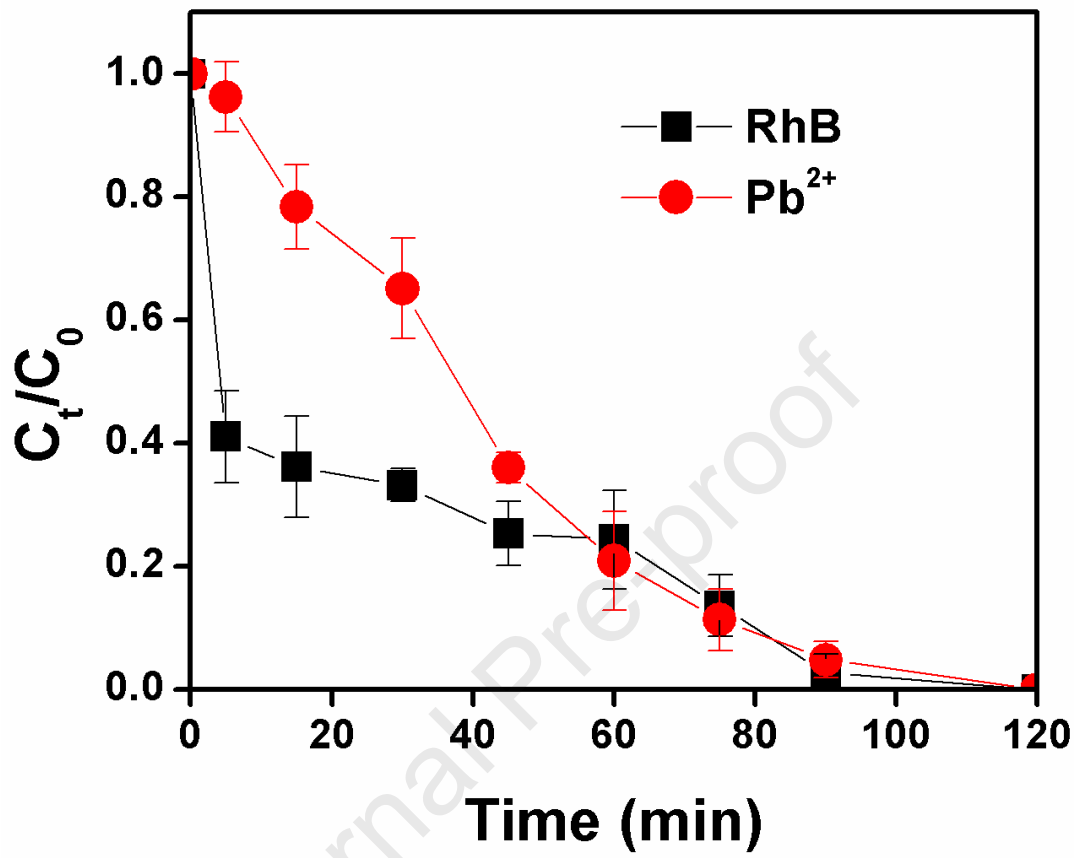


Fig. 5

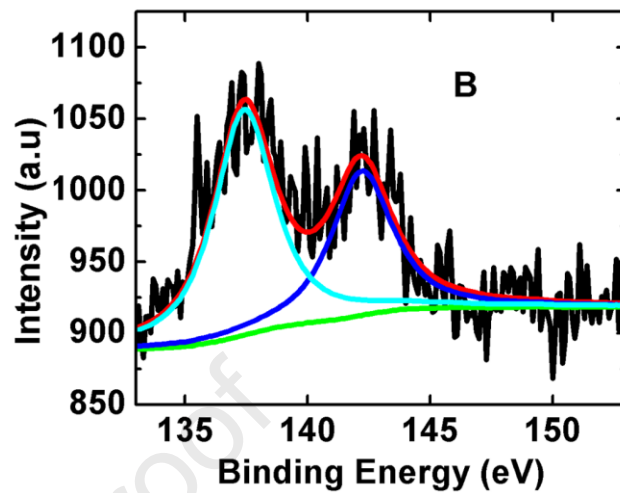
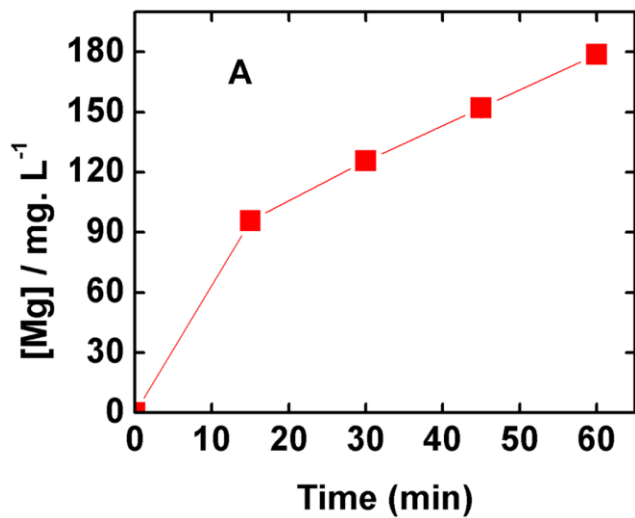


Fig. 6

Journal Pre-proof



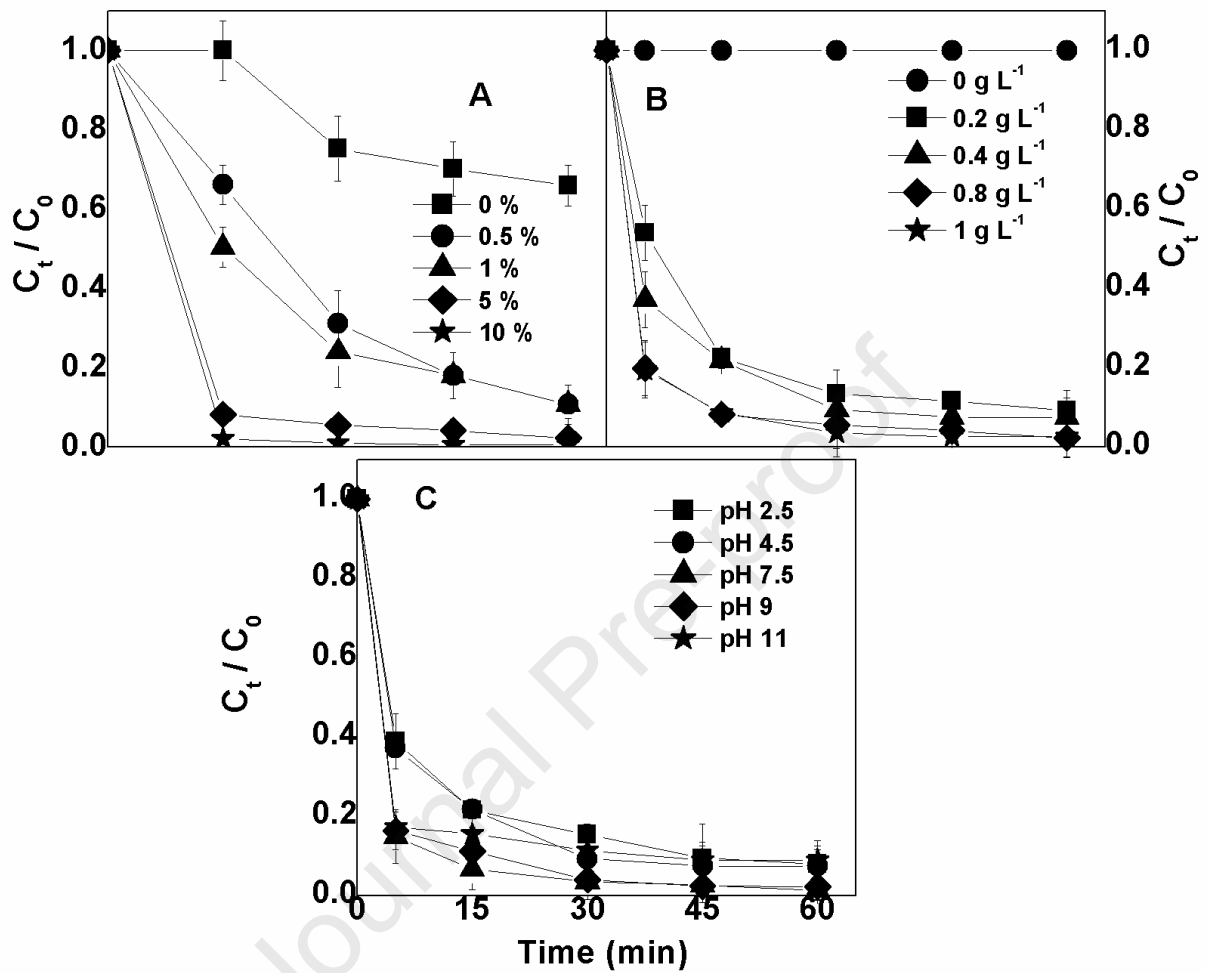


Fig. 7



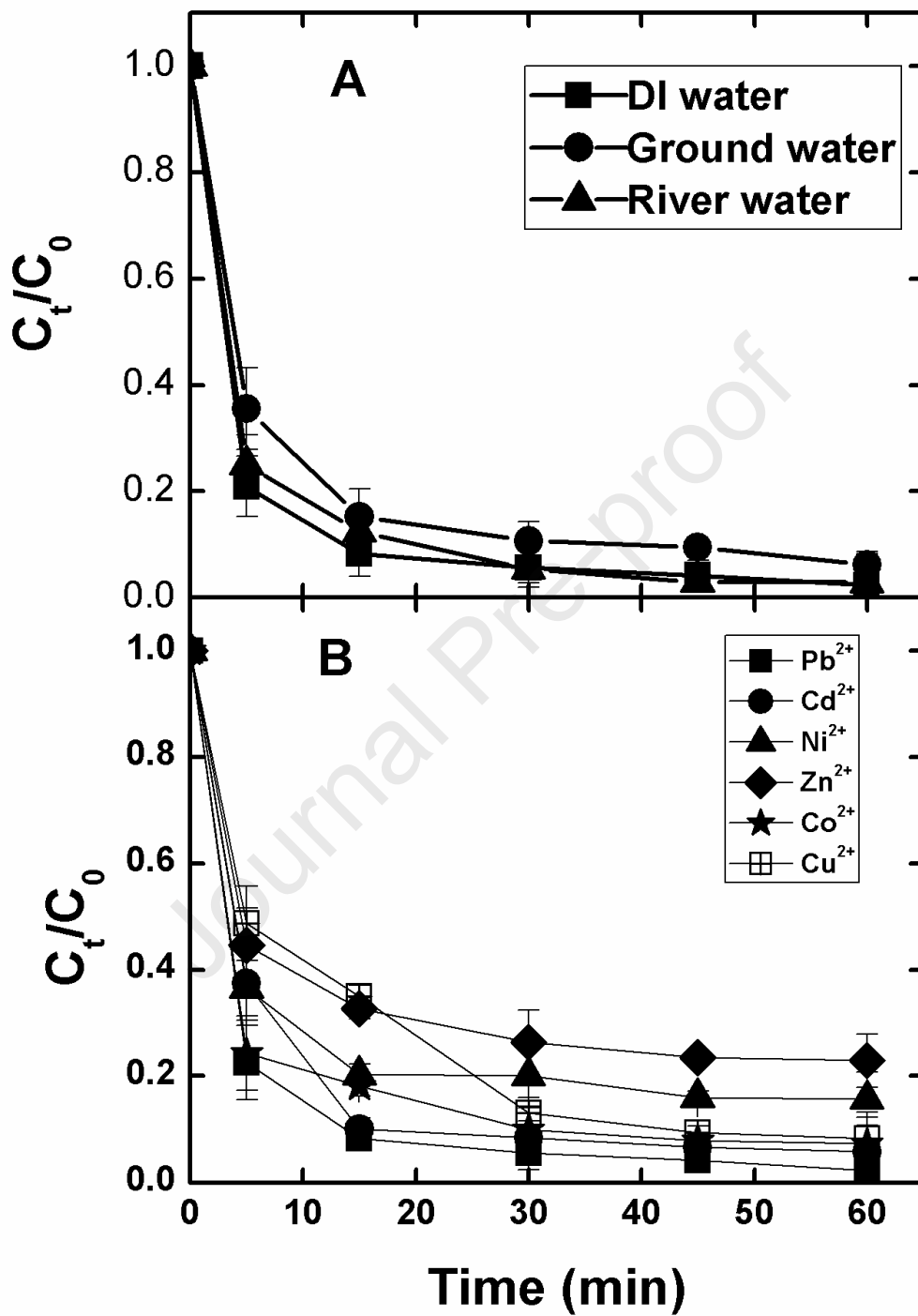


Fig. 8



Highlights

- Heavy metal (Pb^{2+}) and organic dye (Rhodamine B) removal with H_2O_2 addition to the solution containing $\text{Fe}_3\text{O}_4@\text{MgO}$.
- Pollutants are removed by the adsorption mechanism.
- The bubble propulsion and self-mixing process enhanced the removal efficiency.
- $\text{Fe}_3\text{O}_4@\text{MgO}$ is efficient in environmentally relevant water matrices like ground and river water.

Journal Pre-proof